L. Pittarello, S. Goderis, B. Soens, S.J. Mckibbin, G. Giuli, F. Bariselli, B. Dias, B. Helber, G.O. Lepore, F. Vanhaecke, C. Koeberl, T.E. Magin, P. Claeys
Meteoroid Atmospheric Entry Investigated with Plasma Flow Experiments: Petrography and Geochemistry of the Recovered Material
Icarus, Vol. 331, 2019, p. 170-178
doi:10.1016/j.icarus.2019.04.033

Meteoroid atmospheric entry investigated with plasma flow experiments: Petrography and geochemistry of the recovered material

Lidia Pittarello [a, *], Steven Goderis [b], Bastien Soens [b], Seann J. McKibbin [c], Gabriele Giuli [d], Federico Bariselli [e, f, g], Bruno Dias [e], Bernd Helber [e], Giovanni O. Lepore [h], Frank Vanhaecke [i], Christian Koeberl [a, j], Thierry E. Magin [e], Philippe Claeys [b]

[a] Department of Lithospheric Research, University of Vienna, Althanstrasse 14, A-1090 Vienna, Austria
[b] Analytical, Environmental, and Geo-Chemistry (AMGC), Vrije Universiteit Brussel (VUB), Pleinlaan 2, B-1050 Brussels, Belgium
[c] Institute of Earth and Environmental Science, University of Potsdam, Karl-Liebknecht-Str. 24-25, D-14476 Potsdam-Golm, Germany
[d] School of Science and Technology, Geology Division, University of Camerino, Via Gentile III da Varano, I-62032 Camerino, Italy
[e] Aeronautics and Aerospace Department, von Karman Institute for Fluid Dynamics (VKI), Waterloosesteenweg 72, B-1640 Sint-Genesius-Rode, Belgium
[f] Research group Electrochemical and Surface Engineering (SURF), Vrije Universiteit Brussel, Pleinlaan 2, B-1050 Brussels, Belgium
[g] Dipartimento di Scienze e Tecnologie Aerospaziali, Politecnico di Milano, Via La Masa, 34, 20156 Milano, Italy
[h] CNR-IOM-OGG c/o ESRF, 71 Avenue des Martyrs CS 40220, F-38043 Grenoble, France
[i] Atomic and Mass Spectrometry Research Unit, Department of Chemistry, Ghent University, Krijgslaan, 281 - S12, B-9000 Ghent, Belgium
[j] Natural History Museum (NHM), Burgring 7, A-1010 Vienna, Austria

ARTICLE INFO

Keywords:
Melting experiments
Atmospheric entry
Meteorites
Fusion crust
Redox

ABSTRACT

Melting experiments attempting to reproduce some of the processes affecting asteroidal and cometary material during atmospheric entry have been performed in a high enthalpy facility. For the first time with the proposed experimental setup, the resulting material has been recovered, studied, and compared with natural analogues, focusing on the thermal and redox reactions triggered by interaction between the melt and the atmospheric gases under high temperature and low pressure conditions. Experimental conditions were tested across a range of parameters, such as heat flux, experiment duration, and pressure, using two types of sample holders materials, namely cork and graphite. A basalt served as asteroidal analog and to calibrate the experiments, before melting a H5 ordinary chondrite meteorite. The quenched melt recovered after the experiments has been analyzed by μ-XRF, EDS-SEM, EMPA, LA-ICP-MS, and XANES spectroscopy.

The glass formed from the basalt is fairly homogeneous, depleted in highly volatile elements (e.g., Na, K), relatively enriched in moderately siderophile elements (e.g., Co, Ni), and has reached an equilibrium redox state with a lower Fe^{3+}/Fe_{tot} ratio than that in the starting material. Spherical objects, enriched in SiO_2, Na_2O and K_2O, concentrations, were observed, inferring condensation from the vaporized material. Despite instantaneous quenching, the melt formed from the ordinary chondrite shows extensive crystallization of mostly olivine and magnetite, the latter indicative of oxygen fugacity compatible with presence of both Fe^{2+} and Fe^{3+}. Similar features have been observed in natural meteorite fusion crusts and in micrometeorites, implying that, at least in terms of maximum temperature reached and chemical reactions, the experiments have successfully reproduced the conditions likely encountered by extraterrestrial material following atmospheric entry.

1. Introduction

Atmospheric entry of asteroidal and cometary material likely implies melting, evaporation, loss of mass, physical separation of metal-rich phases, and redox variations. All these processes may affect microstructures of and induce chemical changes in the recovered meteorites and micrometeorites. Ablation is an important factor, but if the meteoroid is large enough a portion survives and falls on the Earth

* Corresponding author.
Email address: lidia.pittarello@univie.ac.at (L. Pittarello)

covered by a quenched melt film called fusion crust (e.g., Genge and Grady, 1999a). Similar processes might also affect microscopic dust particles (10–2000 μm) that enter the Earth's upper atmosphere and are recovered on Earth as micrometeorites (e.g., Genge et al., 2008; Rubin and Grossman, 2010), as locally similar features are observed, for example in the form of a melt film coating the surface (e.g., Toppani and Libourel, 2003; Genge, 2006). The degree of melting and therefore the preservation potential of internal features mainly depend on the physico-chemical parameters of the extraterrestrial material (i.e., size, density, composition) and on the entry conditions (i.e., velocity, angle; e.g., Love and Brownlee, 1991). Based on the degree of melting experienced during atmospheric passage by micrometeoroids, the distinction is generally made between fully melted micrometeorites (or cosmic spherules), partially melted micrometeorites (or scoriaceous MMs), and unmelted or angular micrometeorites (e.g., Maurette et al., 1994; Taylor et al., 1998; Genge et al., 2008). Thus, to some degree, analogies may exist between the processes that lead to the formation of cosmic spherules and those that generate meteorite fusion crusts.

Physical effects of atmospheric entry have been investigated both by numerical modeling (e.g., Love and Brownlee, 1991; Dias et al., 2016) and experimentally, in the form of static heating (e.g., Greshake et al., 1998; Toppani et al., 2001), impact ballistics (Thomas and White, 1953; Zotikov, 1959), plasma flow (Shepard et al., 1966; Loehle et al., 2017; Agrawal et al., 2018; Pratesi et al., 2018), and laser (Milley et al., 2007; Stern 2015, personal communication) set-ups. A review of the historical experiments is presented in Helber et al. (subm.). In the past, experimental conditions were generally far from those experienced by planetary material during atmospheric entry in terms of temperature, duration, and employed materials, and so far, only rarely glass could be recovered after the experiments.

In this work, petrographic and geochemical characterization of the quenched melt formed during experiments in the high-enthalpy Plasmatron facility at the von Karman Institute for Fluid Dynamics (VKI) in Sint-Genesius-Rode, Belgium, is presented. As starting material, a terrestrial basalt and an ordinary chondrite (H5) meteorite were used. The resulting glass was then compared with natural meteorite fusion crust and micrometeorites, in an attempt to advance our understanding of the thermal and chemical processes occurring during and following atmospheric entry.

2. Experimental setup, sample description, and analytical methods

The VKI Plasmatron, an induction heated plasma wind-tunnel commonly used to test spacecraft heat shields, can produce a steady-state air plasma flow of over 10,000 K temperature, and a maximum heat flux of 16 MW/m^2. The stagnation point region of a hypersonic body entering the atmosphere, due to the shock wave on the front of the bolide, compresses the air to temperatures exceeding 10,000 K. For this reason, the high velocity typical during atmospheric entry transforms into high total enthalpy. A subsonic ground-test facility, such as the VKI Plasmatron, is thus able to replicate the atmospheric entry flight conditions in a subsonic environment through the so-called Local Heat Transfer Simulation methodology, developed by Kolesnikov (1993). Experiments were performed in the spring of 2016 under the conditions listed in Table 1, using air as source for the plasma flow. Cylindrical samples of diameter 16 mm were cored from raw experimental materials. The sample was held in a protective, water-cooled metallic housing, maintaining a temperature range between room temperature and 70 °C, before injection into the hot plasma flow. During the experiments, the material has been exposed to a cold wall heat flux of 3 MW/m^2 at 15 hPa as well as 1 MW/m^2 at 200 hPa (Table 1), corresponding to enthalpies of approximately 54 and 24 MJ/kg and flow velocities of approximately 687 and 26 m/s, respectively. These conditions reproduce the flight of an object ca. 4 m in diameter, entering with a velocity of ca. 6.5 km/s at an altitude of ca. 55 km. During the experiments, the surface temperature, the temperature of the sample in contact with the holder, and vapor ablation products at the very contact between plasma and sample were directly measured and subsequentely modeled. Further detailed information on the analytical setup is provided in Helber et al. (subm.).

The specimen was placed in a hemispheric holder made of cork or graphite for different sets of experiments (Table 1). The test sample, initially at room temperature and positioned on a water-cooled holding arm, was hydraulically inserted into the plasma flow when the experimental conditions, continuously monitored, had reached the desired state. For the first set of experiments, an alkali-rich basalt was used, in order to enable the possibility of investigating evaporation phenomena of the volatile alkali metals, to act as a general analog for some basaltic achondrite meteorites and micrometeorites, and to serve as a reproducible testing material before subjecting a chondrite meteorite to full test conditions. The selected sample consists of alkali-rich basalt collected in the locality of Château de Pourcheyrolles (France), where columnar basalt occurs from the strombolian volcanic sequence of the Montpezat-sous-Bauzon, Ardèche, active between 65 Ma and 7 ka. This basalt is particularly homogeneous on the scale of a hand sample and consists of clinopyroxene phenocrysts embedded in a feldspathic groundmass, with flow fabric marked by clinopyroxene and ilmenite crystal alignment (Fig. 1a). No sulfides or sulfates were observed. According to our analyses, this alkali-rich basalt can technically be referred to as a tephry-phonolite, according to the classification by Le Bas et al. (1992). Bulk compositional data are provided in the supplemental material. Different experimental conditions were tested on the basalt, to constrain the behavior of the sample, before testing a drilled fragment of ordinary chondrite El Hammami (H5), purchased for this purpose. Ordinary chondrites represent the vast majority of all meteorites recovered on Earth (e.g., Hutchison, 2004; Grady et al., 2014). Among ordinary chondrites, type H represents a relatively reduced chemical composition and, therefore, is suitable to highlight possible redox processes induced by interaction between the melt and the atmospheric oxygen. The selected fragment contains a few relic chondrules, largely recrystallized, coarse-grained olivine ($Fa_{18.8}$), pyroxene ($Fs_{16.7}Wo_{1.4}$), and rare small plagioclase crystals and metal (Grossman, 1998).

The material recovered from experiments B 1.1 (basalt in cork sample holder) and B 1.2 (basalt in graphite sample holder; Table 1) was analyzed using a M4 Bruker Tornado μ-XRF at the Vrije Universiteit Brussel (VUB), Brussels, Belgium, for element mapping and semi-quan-

Table 1
Experimental conditions for the runs considered in this work.

Experiment name	Material	Sample holder	Heat flux (MW/m^2)	Heat flux probe	Pressure (hPa)	Duration (s)
B1.1	Basalt	Cork	3.04	Hemispherical	15	41
B1.2	Basalt	Graphite	3.12	Hemispherical	15	21
B2.1	Basalt	Cork	1.01 (1.2)[a]	Flat (hemispherical)	200	12
OC2.1	Ordinary chondrite	Cork	1.01 (1.2)[a]	Flat (hemispherical)	200	21

[a] Calculated by applying a similarity rule for the heat flux.

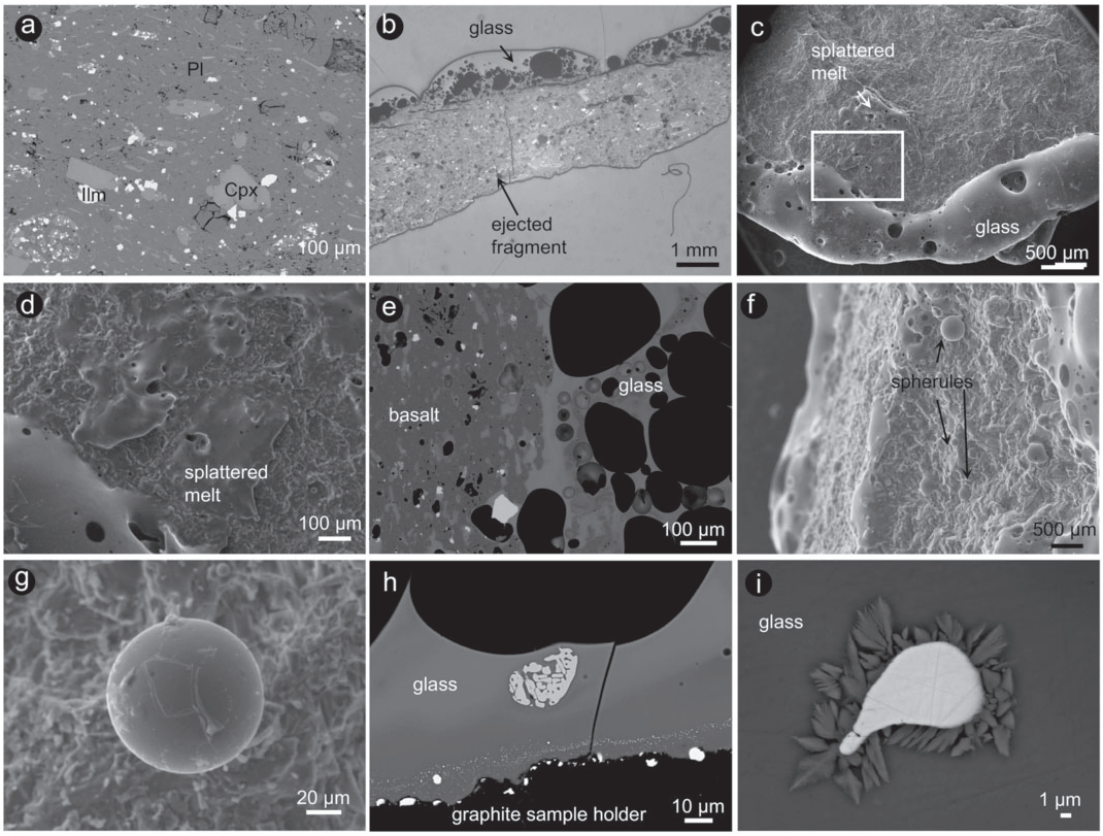

Fig. 1. Basalt before and after the melting experiments. a) BSE-SEM image of the pristine basalt, showing flow fabric marked by aligned clinopyroxene and ilmenite crystals (mineral abbreviations according to Whitney and Evans, 2010). b) Microphotographs of an ejected fragment of basalt coated with vesiculated melt. Reflected light, optical image. Experiment B2.1. c) SE-SEM image of the melt coating the edge of a basalt fragment. Experiment B2.1. d) Detail of (c), showing splattered melt on the surface of the basalt. SE-SEM image. e) BSE-SEM image of the transition between the preserved portion of the basalt and the melt. Experiment B2.1. f) SE-SEM image of the spherical objects. Experiment B2.1. g) Detail of a spherical object. SE-SEM image. h) Trails of metallic Fe-Si alloys crystallizing at the contact with the sample holder in graphite and globular magnetite. BSE-SEM image. Experiment B1.2. i) Microlites, likely of plagioclase, growing over a clast of ilmenite in the melt. BSE-SEM image. Experiment B1.2.

titative chemical analysis, with a Rh beam and spot size of 25 µm. Preliminary observations and rough chemical characterization were also performed with a JEOL JSM IT-300 scanning electron microscope (SEM), equipped with EDS detector, at the VUB. Electron microprobe analysis (EMPA) was performed with a JEOL JXA 8530-F instrument at the Natural History Museum of Vienna, Austria, equipped with five wavelength-dispersive spectrometers (WDS) and one EDS, on polished chips prepared from the material recovered from experiments B1.2, B2.1, and OC2.1 (Table 1). Operative conditions were 15 kV acceleration voltage, 12 nA beam current, and with a fully focused beam. For glassy material, a defocused beam with a spot size of 10 µm was used. For quantification, a ZAF correction was applied and the content was calculated in oxides, except for the metal in the ordinary chondrite. Detection limits for major elements are listed in Table S1 in the Supplemental Material. The composition of olivine ($[Mg,Fe]_2SiO_4$) is expressed as fayalite Fe_2SiO_4 (Fa) mol% (Mg/(Mg + Fe)∗100). The mineral abbreviations Ol for olivine and Fa for fayalite, as well as Mag for magnetite and other abbreviations, are used according to Whitney and Evans (2010). Major and trace element concentrations were additionally determined using a Teledyne Cetac Technologies Analyte G2 ArF* excimer-based laser ablation system coupled to a Thermo Scientific Element XR double-focusing sector field ICP-mass spectrometer (LA-ICP-MS) at the Department of Chemistry of Ghent University, Belgium, following the procedures described in Das Gupta et al. (2017).

The oxidation state of Fe in the basalt before and after the experiments B1.1 and B1.2, as indication of the redox conditions, was determined using Fe K-edge X-ray Absorption Near Edge Structure (XANES) spectroscopy. X-ray absorption spectroscopy (XAS) spectra were collected at the LISA beamline BM08 (d'Acapito et al., 2016, 2017) at the European Synchrotron Radiation Facility (ESRF) in Grenoble (France). All samples were measured in fluorescence mode by means of a 12-element solid state (high-purity Germanium) detector. The monochromator was equipped with a pair of Si [111] flat crystals; higher order harmonics were rejected by using Si-coated focusing mirrors ($E_{cutoff} \approx 15$ keV); beam size on the sample was approximately 200×200 µm^2. The basalt was analyzed as a powder mixed with cellulose and pressed into a pellet, with an amount of material such as to keep the maximum total absorption (µ) below 1.5. From the material after experiment B1.2, XAS data were collected on molten droplets embedded in a resin pellet and then polished. Material recovered after experiment B2.1, due to the low amount of quenched melt available, required manual glass separation, and only after ascertaining the absence of crystalline phases was prepared as powder sputtered onto a kapton tape.

XAS spectra were collected along the Fe K-edge from 200 eV below the edge up to 650 eV after the edge, with variable energy step (0.10 eV across the pre-edge and 0.3 eV on the edge regions). The software ATHENA (Ravel and Newville, 2005) was used to average multiple spectra. Standard procedures (Lee et al., 1981) were followed for pre-edge background removal, spline modeling of bare atomic background, edge step normalization using a far above the edge region, and energy calibration. Pre-edge peak data analysis was done according to the method described in Wilke et al. (2001) and Giuli et al. (2002 and 2011).

3. Results

In all experiments, the plasma flow temperature was estimated to be roughly between 5000 and 9000 K (Helber et al., subm.). The temperature on the surface of the sample, measured and modeled, reached an asymptotic value in the range of 2280–2360 K, regardless of the nature of the material and of the sample holder (Helber et al., subm.). All samples started at room temperature and cooled slightly during pumping down of the test chamber to reach the required vacuum. The temperature gradient throughout the sample material strongly depended on the sample holder material (graphite or cork). In the case of graphite, which is a good thermal conductor, the temperature at the back of the sample rapidly increased by 640 K compared to the initial temperature. In the case of cork, which in contrast to graphite is a good thermal insulator, the temperature at the back of the sample almost did not vary during the experiments, with limited temperature rises differences between only 3 K and 100 K. Nevertheless, all samples exhibited melting, boiling and evaporation during the experiments. Detailed information is provided for the individual experiments.

3.1. Petrographic and geochemical observations in experiments with basalt

The response of the basalt strongly depended on the nature of the sample holder. In the case of cork, the basalt experienced intense fracturing and ejection of material, due to the insulation properties of cork, causing a strong thermal gradient within the sample between the exposed surface and the cold interior. Here, it should be noted that fracturing has been also observed after drying the sample by exposure to 100 °C overnight. In the case of graphite, low-viscosity melt dropped away on the surface of the sample holder and melting also occurred along the sides of the sample, triggered by the high thermal conductivity of graphite. A few mm of sample were lost at the front of the plasma flow by vaporization and removal of melt during the experiments. Upon quenching, the melt appears as a thin (< 500 μm) film of glass coating the preserved basalt, also in ejected fragments from experiment B1.1 (Fig. 1b, c), locally splattered on the surface of the basalt (Fig. 1c, d), as droplets of blackish glass after experiment B1.2. The transition between the preserved portion of basalt and the glass is marked by abundant vesiculation, with vesicles of various size (50 μm–1 mm) (Fig. 1e). Spherical objects, 200–500 μm in size, have formed at the front of the glass film (Fig. 1f, g). In the experiment B1.2, Fe-Si metal alloys crystallized at the contact between the melt and the graphite (Fig. 1h). These alloys have a calculated mineral formula of $Fe_{2.5}Si$, which is in between that of hapkeite (Fe_2Si) and gupeiite (Fe_3Si), both of extraterrestrial origin and observed in lunar soils and likely in metallic cosmic spherules, respectively. Hapkeite has been suggested to form by condensation of impact vaporized phases (Anand et al., 2003). In BSE-SEM images, local *schlieren* and domains with different BSE contrast in BSE-SEM images can be observed (Fig. 1h). Locally, evidence of devitrification and incipient crystallization, with skeletal growth of unidentified phases over relic nuclei, is present (Fig. 1i).

Chemically, the glass formed from the basalt shows overall depletion in volatile alkali metals (40–60% of the original content for Na, 50% for K) and highly volatile elements, with apparent enrichment in more refractory elements (Mg and Ca contents are doubled; Fig. 2a, Tables S2–3). In detail, the difference between the bright and dark glass *schlieren* in BSE images is limited to a more marked enrichment in Ti, Fe, and Mn in the bright domains than in those with darker appearance. The enrichment in Ti, Ca, Mg, Fe, and Mn with a factor 2 or more in the glass is common, regardless of the sample holder. Additionally, in experiment B1.2, a considerable enrichment in Ni (20 times higher than the preserved basalt) and Cr in the glass is observed. Spectroscopic analysis during the experiments indicates that Na, K, Mg, Ca, Fe, and Ti are volatilized, but the relative abundance could not be unambiguously determined, because both the cork and the graphite produced a strong K and Na emission in addition to those from the samples (Helber et al., subm.). Relative to the pristine basalt before the experiments, the glass is enriched in rare earth elements (REE) and Y (Fig. 2b) and in moderately siderophile elements, such as Co, Ni, and Cu (Table S5). Among the spherical objects, two populations can be distinguished for their size. While the observed larger objects (Fig. 1f, g) have a clear, relatively "feldspathic" composition (Table S2), the composition of smaller objects was difficult to be determined, due to contamination from the surrounding unmelted basalt. According to the pre-edge peak analysis of XAS data (reported in Fig. 3), the glass in both experiments B1.2 and B2.1 (0.17 ± 0.05 and 0.11 ± 0.05, respectively) exhibits a lower Fe^{3+}/Fe_{tot} ratio than that in the original basalt (0.75 ± 0.15).

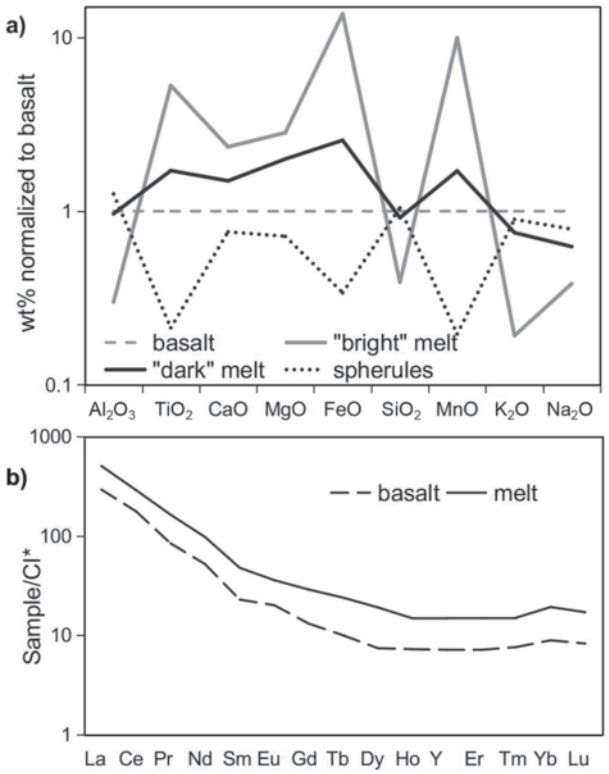

Fig. 2. Chemical differences of the melt with respect to the original basalt. a) Major element content, plotting the elements according to the 50% condensation temperature (after Lodders, 2003). b) REE and Y contents in the basalt before the experiment and in the melt, averaged between experiment B1.2 and B2.1, normalized to CI chondritic abundances (McDonough and Sun, 1995).

3.2. Petrographic and geochemical observations in the experiment with the ordinary chondrite

The meteorite sample experienced only melting and limited evaporation during the experiment. No material was ejected or escaped from the sample holder. The resulting glass displays large vesicles and coats the exposed surface of the sample (Fig. 4a). There is no sharp transition between the unaffected interior of the meteorite sample and the molten and quenched portion and the glass is largely crystallized.

Olivine crystals in contact with the glass exhibit cracks filled by glassy melt, trails of metal-rich inclusions, and an overgrown rim with a higher Mg/Fe ratio than that of the host olivine (relative average Mg# from 81 to 85; Fig. 4b, Table S4). The glass resulting from the

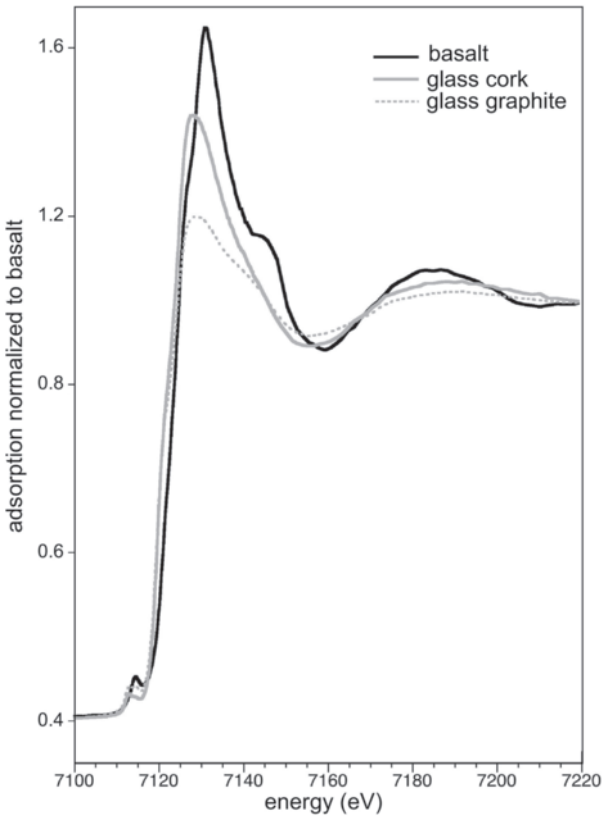

Fig. 3. Fe K-edge XANES spectra of the starting basalt (black line) and the glass produced by melting with a cork sample holder (continuous grey line) and with a graphite sample holder (dotted grey line). The edge energy of the glass samples has lower values than that of the basalt, due to a lower Fe oxidation state.

experiment is dominated by olivine showing a variety of morphologies, including tabular, skeletal, and hopper crystal shapes (Fig. 4c–e), consistent with the olivine morphology description from quenched melt in Faure et al. (2003). Relict olivine clasts exhibit evidence of incipient melting and overgrowth of sub-euhedral rims (Fig. 4c). Such rims represent inverse zoning with respect to the host olivine, as their composition at the contact with the host olivine is more enriched in Mg than that in the preserved nucleus. The rim composition eventually evolves into normal zoning, showing a progressive change of the Mg/Fe ratio towards more Fe-rich compositions at the contact with the glassy groundmass (Mg# from 85 to 75 on average; Fig. 4b–d; Table S4). In the groundmass, skeletal magnetite has crystallized (Fig. 4e). In the interior of the meteorite, kamacite and taenite appear in coarse-grained exsolution bands. In the quenched melt, only botryoidal kamacite, with higher Ni content than in the interior of the meteorite (from ca. 6 wt% to 12 wt% on average), occurs, set within a troilite groundmass (Fig. 4f). Locally, fine-grained, skeletal crystals of chromite occur (Fig. 4g). Fig. 4h and i shows the corresponding features in natural fusion crusts of H-chondrites.

The quenched melt from the experiment with ordinary chondrite, considered as bulk, (including the crystals) is overall slightly enriched in Ti, Fe, and Cr, with moderate siderophile element variations, and slight depletion in volatile elements, such as K and Na, which were present in low amounts in the pristine material, as semi-quantitatively evaluated, considering the high analytical uncertainties due to the coarse grained nature of the crystalline phases (Tables S4–6). The REE and Y contents in the glass are depleted with respect to the original chondrite, contrasting the observations made for the experiments involving basalt (Fig. 5a). The concentrations of the moderately siderophile elements (Co, Ni, Cu) are highly variable and difficult to interpret, likely due to the large internal variability in the ordinary chondrite data (Table S5) and to the limited laser beam diameter during LA analysis (50 μm) in comparison to the coarse grain crystal size in the ordinary chondrite (e.g., Fig. 4).

Olivine that crystallizes from the melt can be subdivided into two populations on the basis of the MgO content with respect to the olivine in the interior of the meteorite (Fig. 5b). However, both populations exhibit similar enrichment in refractory elements, such as (Al, Cr, Ni, Ca, but not Ti) with apparent depletion in the moderately volatile elements and Mn. In particular, newly crystallized olivine seems to contain "impurities", such as Cr, Ni, and Ca, even though this might be apparent and due to analytical limitations. In fact, the apparent enrichment in Na and Al is likely related to local contamination from the groundmass, due to the size of the analyzed material (olivine rims have a thickness of a few μm; Fig. 4) with respect to the interaction volume of the electron microprobe beam (also on the order of some μm; Table S4).

4. Discussion

4.1. Melting, evaporation, and condensation

In all experiments, regardless of the nature of the material and of the sample holder, the resulting glass composition clearly shows minor enrichment in some moderately refractory elements (e.g., Ti and Ca) and relative depletion in highly volatile elements (such as K and Na). The evaporation of highly volatile alkali metals is particularly obvious in the case of the basalt, as the selected basalt has significantly higher concentrations of Na_2O (6.7 wt%) and K_2O (5.8 wt%; Table S2) relative to the H chondrite (Na_2O of 1.6 wt% and K_2O of 0.15 wt%; Table S6). The formation of vesicles in both the basaltic and chondritic glasses is obviously related to the vaporization of such highly volatile elements (50% condensation temperature T_c of 958 K and 1006 K for Na and K, respectively; Lodders, 2003) with a possible contribution from elements such as Fe (50% T_c of 1334 K; Lodders, 2003). The latter element was detected by spectroscopic analyses and is observed as Fe-oxide condensates along the rims of the vesicles. Vesiculation is commonly observed in natural meteorite fusion crusts (e.g., Genge and Grady, 1999a; Pittarello et al., 2019), but also in micrometeorites (e.g., Genge, 2016b; Suttle et al., 2019), where a high content of volatiles in the original precursor material has been invoked to explain vesicle formation. In the case of the basalt, a high abundance of volatiles, such as water and halogens, is likely present. However, this is not the case for the ordinary chondrite, which in contrast to carbonaceous chondrites is relatively dry (e.g., Breaerly, 2006). The quenched melt in the experiments does not display any lateral variation reflecting melting of local phases but is rather homogeneous. This observation is consistent with what observed in natural fusion crusts of H5 chondrites (Pittarello et al., 2019) and in contrast with previous works (e.g., Genge and Grady, 1999a; Thaisen and Taylor, 2009). However, in the case of the experiments, the small sample size and the geometry of the experiments favor mixing and homogenization. In natural fusion crusts, homogenization may be additionally aided by the spinning of the meteorite during flight.

The origin of the spherical objects found at the interface of the glass formed from the basalt remains unclear. In some cases, chemical compositions rich in alkali metals and silica might suggest possible condensation of vaporized phases. No spherical objects were observed in the glass obtained from the ordinary chondrite. In natural fusion crust, a possible ablation spherule, with a composition close to that of the bulk chondrite, was observed (Pittarello et al., 2019). This suggests that the observed spherical objects on the surface of the basaltic glass formed by a different mechanism than meteorite ablation spherules.

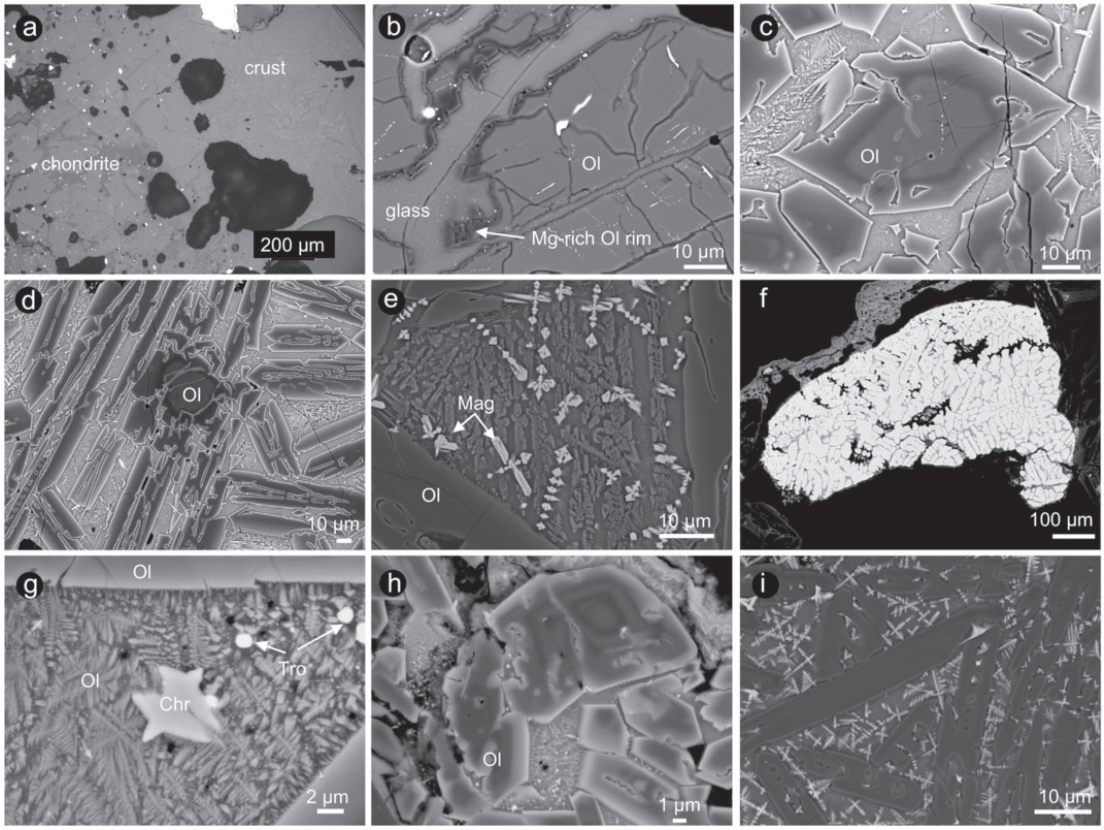

Fig. 4. Melt formed in the experiment OC2.1, from a fragment of the H5 ordinary chondrite El Hammami, and comparison with natural meteorite fusion crust. a) Microphotograph of the thin chip used for analysis, showing the interior of the meteorite and the vesiculated melt. Reflected light, optical image. b) BSE-SEM image of the transition zone between the unaffected interior of the meteorite and the melt, showing olivine crosscut by cracks and by trails of opaque phases and with a darker rim towards an apparently homogeneous melt. c) BSE-SEM image of olivine relic clast exhibiting overgrowth from the melt with initial crystallization of Mg-rich olivine, followed by crystallization of progressively more Fe-rich olivine. Note the fine grained skeletal phases crystallized in the melt. d) BSE-SEM image of hopper and skeletal olivine crystallizing from the melt. e) BSE-SEM image of the groundmass between new crystals of olivine, with skeletal magnetite and likely olivine. f) BSE-SEM image of a metal bleb in the melt consisting of botryoidal kamacite in a troilite matrix. g) BSE-SEM image of a chromite crystal in a groundmass consisting of likely skeletal olivine, troilite blebs, and glass. h) BSE-SEM image of zoning in olivine clasts and crystals in the Antarctic meteorite Asuka 09502, classified as H5 (Pittarello et al., in review). Note the similarity with (c). i) BSE-SEM image of hopper olivine with skeletal magnetite in the groundmass in the Antarctic meteorite Asuka A 09004, classified as H5 (Pittarello et al., in review). Note the similarity with (e).

Moderately siderophile elements, such as Co, Ni, and Cu are enriched in the glass formed in all the experiments. Partitioning of such elements between melt and silicates may be controlled by the oxygen fugacity (Gaetani and Grove, 1997). In this case, the partitioning would be between vapor and melt. The enrichment in moderately siderophile elements shown in the glass is likely the result of the evaporation of the more volatile elements. However, despite the relatively large uncertainties associated with these analyses, simple mass balance calculations suggest passive enrichment not to be the sole cause for the observed concentration ranges.

4.2. Redox processes

For the selected basalt, Log f(O_2) was estimated with the software MAGMA (Schaefer and Fegley, 2004), yielding −4 at 2200 K, which is close to the temperature reached during the experiments. Oxygen partial pressure in the gas during the experiment can be calculated. Such estimates suggest high f(O), such as Log f(O) −1.25 and Log f(O_2) −4.86 on the assumption of finite rate chemistry at boundary, and Log f(O_2) −1.41 assuming chemical equilibrium, which represents a relatively oxidizing environment during the experiments. This is valid if we ignore the potential reducing effect induced by the presence of graphite and the organic matter in the sample holder, although the geometry of the experiment ensures that any interaction between the melt and the sample holder is generally avoided, except at the very contact between the two. This local effect is negligible in the scope of the overall redox reactions. The Fe^{3+}/Fe_{tot} ratios observed in the experiment B1.2 with graphite sample holder ($Fe^{3+}/Fe_{tot} = 0.17 \pm 0.05$) and in experiment B2.1 with cork sample holder ($Fe^{3+}/Fe_{tot} = 0.11 \pm 0.05$) are very close to those calculated according to the Kress and Carmichael (1991) model using the glass composition, the estimated T and oxygen fugacity conditions of the experiment. This correspondence suggests that the melt was in equilibrium (or close to equilibrium) with the surrounding atmosphere. Despite the short duration of the experiments, it is not surprising that equilibrium can be achieved for the Fe redox reaction, because at extremely high temperature, as recorded during the experiments, Fe redox kinetics are extremely fast. In an experiment, where basalt was molten at ca. 1770 K, equilibrium was reached after 66 s (Cicconi et al., 2015). The experimental data indicate that at such high temperature the produced melt can quickly equilibrate with the surrounding medium and, for the conditions used here, produce a melt where Fe^{2+} and Fe^{3+} coexist (in our case with the Fe^{3+}/Fe_{tot} ratio ranging between 0.11 and 0.17). These data are compatible with the formation of magnetite in the produced chondrite melt, where the oxygen fugacity in H chondrites has been calculated to be ca. Log f(O_2) −20 at 800 °C (Rubin et al., 1988). It must be noted that, as the melt achieved equilibrium, the resulting Fe_{3+}/Fe_{tot} ratio would have been the same regardless if the starting material was more oxidized (as in the basalt case) or more reduced (as in the meteorite case).

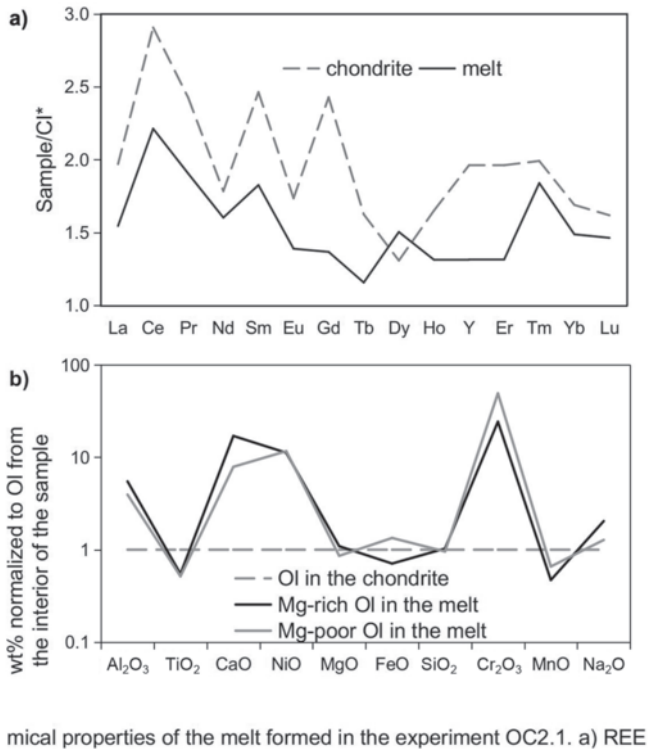

mical properties of the melt formed in the experiment OC2.1. a) REE

Fig. 5. Chemical properties of the melt formed in the experiment OC2.1. a) REE and Y contents in the interior of the meteorite (OC) and in the melt, normalized to CI chondritic abundances (McDonough and Sun, 1995). b) Olivine composition in the melt compared to that in the interior of the meteorite. Oxides ordered according to the 50% condensation temperature (Lodders, 2003).

Experiments with sample holders of different materials, namely graphite and cork, were performed to control the possible influence of sample holders on the resulting glass. While graphite is a good heat conductor, cork is a good insulator. Chemically, both contain carbon, a potentially reducing agent, but because of their individual thermal response, carbon is released under different conditions. The thermal properties of the two materials affected the temperature rise of the samples at the exposed surfaces (Table 1), as the basalt embedded in graphite reached boiling temperatures much earlier than that inserted in cork. At a local scale, at the direct contact between the quenched melt and the graphite, metal droplets (Fe-Si alloys) crystallized (Fig. 1h), suggesting that the interaction between the still hot melt and graphite induced chemical reduction of the melt. However, considering the geometry of the experimental set up, the glass not in direct contact with the graphite holder should not have been chemically affected by the sample holder.

The redox process is more complex in the case of the ordinary chondrite, which was originally relatively reduced (e.g., Rubin et al., 1988), and contains metallic Fe and Ni. Nevertheless, considering olivine crystallization as a proxy for the redox process occurring in the melt, an initial reduction is indicated by the occurrence of olivine compositions at the direct contact with relict olivine crystals with higher Mg/Fe ratios than those of olivine crystals in the interior of the meteorite. However, this observation might reflect the melt temperature, as Mg-rich terms have higher crystallization temperature than the Fe-rich terms. Nevertheless, in experiment OC2.1, oxidation is the dominant process, as suggested by the crystallization of magnetite in the groundmass, the absence of taenite in the melt, and the growth of Fe-rich olivine at the outer rim of relict olivine fragments in the melt or as dendrites (Fig. 4). Even though no significant variations in the amount of magnetite have been observed in this experiment, previous works have related the abundance of magnetite in the groundmass to the extension of oxidation, suggesting that oxidation shows a gradient from the interior of the meteorite to the fusion crust (e.g., Genge and Grady, 1999a, 1999b). Additionally, we have identified $<5\,\mu m$ skeletal chromite grains in the quench melt of our ordinary chondrite sample. Chromite is essentially absent in low grade type-3 ordinary chondrites, but grew during metamorphism in the ordinary chondrite parent body/ies and is present as relatively large ($\sim$50–100 μm) anhedral grains in higher grade specimens such as our test sample (Ramdohr, 1967; Huss et al., 1981; Rubin, 2003; Wlotzka, 2005). Although it is possible that the grains we have found may represent surviving relicts, their small size and skeletal structure seem to imply fast crystallization from the experimentally produced melt (albeit possibly over relict chromite nuclei). Such chromite grains may indicate further oxidation of Cr^{2+} originally hosted in silicate minerals to Cr^{3+} and the stabilization of chromite in the newly formed melt.

In conclusion, our observations that (i) the basaltic glass is generally "reduced" with respect to the highly oxidized pristine basalt and that (ii) magnetite and Fe-rich olivine rims occurs in the chondritic glass, indicating oxidation of the originally relatively reduced ordinary chondrite, all point to an equilibrium redox condition proper of the experimental setup. This equilibrium condition is rapidly reached at high temperature, within the duration of the experiment. The characteristic oxidation state of the experimental setup is intermediate between that of the basalt and that of the chondrite. Disregarding the original oxidation state of the material, the equilibrium depends on temperature, composition and oxygen fugacity, and it is reached by varying of the relative amounts of Fe^0 (in the chondrite), Fe^{2+}, and Fe^{3+}.

4.3. Comparison with meteorite fusion crust, ablation spherules, and melted micrometeorites

The experiment OC2.1 aimed to reproduce meteorite fusion crust by simulating atmospheric entry of a fragment of ordinary chondrite. The quenched melt produced in the experiment presents the same features observed in natural meteorite fusion crusts from chondrites (for a detailed description, see Genge and Grady, 1999a; and Pittarello et al., 2019), such as extensive crystallization of olivine, the presence of magnetite in the groundmass, and the peculiar zoning in the overgrown olivine (Fig. 3). The extensive crystallization of the melt after experiment OC2.1 was not expected, considering the contrasting conditions with respect to the natural atmospheric entry, such as the duration of the experiment (seconds vs. minutes), and the size of the sample (14 mm in diameter of exposed surface). However, the cooling rate seems to have been similar to that experienced by meteoroids, allowing crystallization of olivine. Thus, based on a comparison of the resulting material with the natural samples, the experiment successfully reproduced the (chemical) conditions encountered by asteroidal material when entering Earth's atmosphere.

Micrometeoroids experience partial (similarly to regular meteoroids) to complete melting (i.e., cosmic spherules), involving evaporation of (moderately) volatile components, oxidation of Fe-Ni alloys to Fe oxides (such as magnetite or wüstite, whose presence has been used to determine the oxygen fugacity), reduction of Fe and formation of immiscible metal beads when the precursor material is particularly enriched in carbon, and loss of siderophile and potentially chalcophile elements as a result of Fe-Ni metal and sulfide bead mechanical ejection or spinel group mineral expulsion (e.g., Taylor et al., 2005; Cordier et al., 2011; Genge, 2016a). Evaporation in cosmic spherules can reach up to 60%–90% in the Ca-Al-Ti-rich (therefore, more refractory) terms, depending on the original composition (Herzog et al., 1999; Alexander et al., 2002; Engrand et al., 2005; Taylor et al., 2005; Cordier et al., 2011), however, condensation products have never been identified in micrometeorites. More recent studies have highlighted that the pres-

ence of volatile elements in micrometeorites might be responsible for the fracturing and heating of particles during atmospheric entry, favoring interaction with atmospheric gases (e.g., Suttle et al., 2019).

The most important process controlling the melt evolution during the atmospheric entry is the oxidation of Fe. This mostly implies the formation of magnetite crystals and, locally, the formation of new, relatively FeO-rich olivine, generally overgrowing pre-existing olivine crystal nuclei (Genge et al., 1997; Genge and Grady, 1999a, 1999b; van Ginneken et al., 2017), similarly to what is observed in meteorite fusion crust and in the experiment OC2.1. However, reduction processes may play an important role during the atmospheric entry of micrometeoroids when the precursor material is particularly rich in carbon (e.g., Genge and Grady, 1999a). This leads to the formation of carbon and metal-rich liquids that are immiscible with the surrounding silicate melt and tend to be ejected from the host material (i.e. pyrolysis; Genge and Grady, 1998).

The maximum temperature achieved during atmospheric entry of micrometeoroids might have been different from that reached in the experiments (ca. 2200 K in the experiments vs. likely 900–2000 K for micrometeoroids; e.g., Love and Brownlee, 1991; Taylor et al., 2000), as well as the oxygen fugacity related to the altitude, where melting can occur for the specific material. Additionally, micrometeorites experience peak heating at much higher altitudes in the atmosphere, where the partial pressure of oxygen is significantly lower (e.g., Genge, 2016a; Genge et al., 2017). This implies that a direct comparison between the results of the experiments presented here and the features contained in micrometeorites might not be completely appropriate. Further experiments, using several precursor materials (including carbonaceous and iron meteorites) are planned in the attempt to reproduce the variety of textural, chemical and isotopic features observed in micrometeorites.

5. Conclusions

The quenched melt recovered from a series of melting experiments in a plasma facility, involving both basaltic and ordinary chondritic starting materials, provides constraints on the thermal and chemical processes that affect extraterrestrial material during atmospheric entry. Chemically, the composition of the resulting glass is depleted in highly volatile alkali metals and slightly enriched in moderately siderophile elements. In the experiments involving the alkali basalt, spherules derived from the condensation of the volatilized elements were observed. In terms of redox reaction, the selected experimental conditions affect the redox state of the samples. Regardless of the initial conditions of the starting material, equilibrium between the sample and the surrounding medium is rapidly reached. For this reason, the terrestrial basalt (with a starting Fe^{3+}/Fe_{tot} ratio of 0.75) has been reduced to a Fe^{3+}/Fe_{tot} ratio of 0.11–0.17 ± 0.05, within the stability field of olivine + magnetite. In contrast, the chondrite is oxidized, as suggested by the crystallization of magnetite, which indicates the presence of Fe^{3+}. However, the path to reach this equilibrium might have not been linear, with possible reduction during the initial stages of melting in the ordinary chondrite. In general, the microstructures observed in the material recovered after experiment OC2.1, with an H5 ordinary chondrite, compare well to whose present in melted micrometeorites and in natural meteorite fusion crusts from the same type of chondrite. As the experiments have demonstrated to have successfully reproduced the features observed in natural samples, the thermal and redox conditions likely encountered by meteoroids during atmospheric entry have been closely approximated by our experiments.

Acknowledgments

Nadine Mattielli of the Université Libre de Bruxelles is thanked for providing the basalt used as meteorite analogue. The authors thank Luiza Zavalan, former student at the VKI, for her help in designing the experiments. Dan Topa und Julia Roszjar are thanked for assistance with the EMPA at the Natural History Museum in Vienna, Austria. The authors thank Matthew Genge and Giovanni Protesi for insightful review comments that greatly helped to improve the manuscript.

Funding

This work was sponsored by the Belgian Science Policy Office (BELSPO), under the Belgian Research Action through Interdisciplinary Networks (BRAIN) funding CONTRAT BR/143/A2/METRO. LP is funded by the Austrian Science Fund (FWF), project V-505 N 29. FB and BS were funded by PhD grants of the Research Foundation - Flanders (FWO), while BD was supported by a PhD grant of the Funds for Research Training in Industry and Agriculture (FRIA). PhC and SG acknowledge the support of the VUB Strategic Research Program and thank BELSPO and the FWO for funding. FV thanks BOF-UGent for financial support under the form of a GOA grant. XAS data collection was granted by the Programma Nazionale delle Ricerche in Antartide ("Meteoriti Antartiche" project ID: PNRA16_00029).

Appendix A. Supplementary data

Supplementary data to this article can be found online at https://doi.org/10.1016/j.icarus.2019.04.033.

References

Agrawal, P., Jenniskens, P.M., Stern, E., Arnold, J., Chen, Y.K., 2018. Arcjet ablation of stony and iron meteorites. In: Proceedings of the Aerodynamic Measurement Technology and Ground Testing Conference (AIAA), Atlanta, Georgia. https://doi.org/10.2514/6.2018-4284.

Alexander, C.M.O'.D., Taylor, S., Delaney, J.S., Ma, P., Herzog, G.F., 2002. Mass-dependent fractionation of Mg, Si, and Fe isotopes in five stony cosmic spherules. Geochim. Cosmochim. Acta 66, 173–183.

Anand, M., Taylor, L.A., Nazaraov, M.A., Shu, J., Mao, H.-K., Hemley, R.J., 2003. New lunar mineral HAPKEITE*: Product of impact-induced vapor-phase deposition in the regolith?. In: 34th Lunar and Planetary Science Conference, Abs. # 1818, Housron, TX, USA.

Breaerly, A.J., 2006. The action of water. In: Lauretta D. S., D.S., Mc Sween Jr, H.Y. (Eds.), Meteorites and the Early Solar System II. University of Arizona, Tucson, pp. 587–624.

Cicconi, M.R., Neuville, D.R., Tannou, I., Baudelet, F., Floury, P., Paris, E., Giuli, G., 2015. Competition between two redox states in silicate melts: an in-situ experiment at the Fe K-edge and Eu L3-edge. Am. Mineral. 100, 1013–1016.

Cordier, C., Folco, L., Suavet, C., Sonzogni, C., Rochette, P., 2011. Major, trace element and oxygen isotope study of glass cosmic spherules of chondritic composition: the record of their source material and atmospheric entry heating. Geochim. Cosmochim. Acta 75, 5203–5218.

d'Acapito, F., Trapananti, A., Puri, A., 2016. LISA: the Italian CRG beamline for X-ray absorption spectroscopy at ESRF. J. Phys. Conf. Ser. 712, 012021https://doi.org/10.1088/1742-6596/712/1/012021.

d'Acapito, F., Lepore, G.O., Puri, A., 2017. The new LISA beamline at the ESRF: an opportunity for environmental sciences. In: Marcelli, A., Maggi, V. (Eds.), Aerosols in Snow and Ice. Markers of Environmental Pollution and Climatic Changes: European and Asian Perspectives. vol. 12, Superstripes Press, Rome, Italy, pp. 45–46.

Das Gupta, R., Banerjee, A., Goderis, S., Claeys, Ph., Vanhaecke, F., Chakrabarti, R., 2017. Evidence for a chondritic impactor, evaporation-condensation effects and meting of the Precambrian basement beneath the "target" Deccan basalts at Lonar crater, India. Geochim. Cosmochim. Acta 215, 51–75.

Dias, B., Bariselli, F., Turchi, A., Frezzotti, A., Chatelain, Ph., Magin, Th., 2016. Development of a melting model for meteors. AIP Conf. Proc. 1786, 160004, (8 pp.) https://doi.org/10.1063/1.4967661.

Engrand, C., McKeegan, K.D., Leshin, L.A., Herzog, G.F., Schnabel, C., Nyquist, L.E., Brownle, D.E., 2005. Isotopic compositions of oxygen, iron, chromium and nickel in cosmic spherules: toward a better comprehension of atmospheric entry heating effects. Geochim. Cosmochim. Acta 69, 5365–5385.

Faure, F., Trolliard, G., Nicollet, C., Montel, J.M., 2003. A developmental model of olivine morphology as a function of cooling rate and the degree of undercooling. Contrib. Mineral. Petrol. 145, 251–263.

Gaetani, G.A., Grove, T.L., 1997. Partitioning of moderately siderophile elements among olivine, silicate melt, and sulfide melt: constraints on core formation in the Earth and Mars. Geochim. Cosmochim. Acta 61, 1829–1846.

Genge, M.J., 2006. Igneous rims on micrometeorites. Geochim. Cosmochim. Acta 70, 2603–2621.

Genge, M.J., 2016. The origins of I-type spherules and the atmospheric entry of iron micrometeoroids. Meteorit. Planet. Sci. 51, 1063–1081.

Genge, M.J., 2016. Vesicle dynamics during the atmospheric entry heating of cosmic spherules. Meteorit. Planet. Sci. 52, 443–457.

Genge, M.J., Grady, M.M., 1998. Melted micrometeorites from Antarctic ice with evidence for the separation of immiscible Fe-Ni-S liquids during entry heating. Meteorit. Planet. Sci. 33, 425–434.

Genge, M.J., Grady, M.M., 1999. The fusion crusts of stony meteorites: implications for the atmospheric reprocessing of extraterrestrial materials. Meteorit. Planet. Sci. 34, 341–356.

Genge, M.J., Grady, M.M., 1999. Unequilibrated assemblages of sulfide, metal and oxide in the fusion crusts of the enstatite chondrite meteorites. Mineral. Mag. 63, 473–488.

Genge, M.J., Grady, M.M., Hutchison, R., 1997. The textures and compositions of fine-grained Antarctic micrometeorites: implications for comparisons with meteorites. Geochim. Cosmochim. Acta 61, 5149–5162.

Genge, M., Engrand, C., Gounelle, M., Taylor, S., 2008. The classification of micrometeorites. Meteorit. Planet. Sci. 43, 497–515.

Genge, M.J., Davies, B., Suttle, M.D., van Ginneken, M., Tomkins, A.G., 2017. The mineralogy and petrology of I-type cosmic spherules: implications for their sources, origins and identification in sedimentary rocks. Geochim. Cosmochim. Acta 218, 167–200.

Giuli, G., Pratesi, G., Paris, E., Cipriani, C., 2002. Fe local structure in tektites and impactites by EXAFS and high-resolution XANES spectroscopy. Geochim. Cosmochim. Acta 66, 4347–4353.

Giuli, G., Paris, E., Hess, K.-U., Dingwell, D.B., Cicconi, M.R., Eeckhout, S.G., Fehr, K.T., Valenti, P., 2011. XAS determination of the Fe local environment and oxidation state in phonolite glasses. Am. Mineral. 96, 631–636.

Grady, M., Pratesi, G., Moggi Cecchi, V., 2014. Atlas of Meteorites. vol. 373, Cambridge University Press, Cambridge, UK.

Greshake, A., Klöck, W., Arndt, P., Maetz, M., Flynn, G.J., Bajt, S., Bischoff, A., 1998. Heating experiments simulating atmospheric entry heating of micrometeorites: clues to their parent body sources. Meteorit. Planet. Sci. 33, 267–290.

Grossman, J.N., 1998. The meteoritical bulletin no. 82, 1998 July. Meteorit. Planet. Sci. 33, A221–A239.

Helber, B., Dias, B., Bariselli, F., Zavalan, L.F., Pittarello, L., Goderis, S., Soens, B., McKibbin, S.J., Claeys, Ph., Magin, T.E., 2019. Analysis of meteoroid ablation based on plasma wind-tunnel experiments, surface characterization, and numerical simulations. Astrophys. J.(subm.).

Herzog, G.F., Xue, S., Hall, G.S., Nyquist, L.E., Shih, C.-Y., Wiesmann, H., Brownlee, D.E., 1999. Isotopic and elemental composition of iron, nickel and chromium in type I deep-sea spherules: implications for origin and composition of the parent micrometeoroids. Geochim. Cosmochim. Acta 63, 1443–1457.

Huss, G.R., Keil, K., Taylor, G.J., 1981. The matrices of unequilibrated ordinary chondrites: implications for the origin and history of chondrites. Geochim. Cosmochim. Acta 45, 33–51.

Hutchison, R., 2004. Meteorites: A Petrologic, Chemical and Isotopic Synthesis. Cambridge University Press, Cambridge, UK, (506 p).

Kress, V.C., Carmichael, I.S.E., 1991. The compressibility of silicate liquids containing Fe_2O_3 and the effect of composition, temperature, oxygen fugacity and pressure on their redox states. Contrib. Mineral. Petrol. 108, 82–92.

Le Bas, M.J., Le Maitre, R.W., Woolley, A.R., 1992. The construction of the total alkali-silica chemical classification of volcanic rocks. Mineral. Petrol. 46, 1–22.

Lee, P.A., Citrin, P.H., Eisenberger, P.T., Kincaid, B.M., 1981. Extended X-ray absorption fine structure - its strengths and limitations as a structural tool. Rev. Mod. Phys. 53, 769–806.

Lodders, K., 2003. Solar System abundances and condensation temperatures of the elements. Astrophys. J. 591, 1220–1247.

Loehle, S., Zander, F., Hermann, T., Eberhart, M., Meindl, A., Oefele, R., Vaubaillon, J., Colas, F., Vernazza, P., Drouard, A., 2017. Experimental simulation of meteorite ablation during Earth entry using a plasma wind tunnel. Astrophys. J. 837, 112–121.

Love, S.G., Brownlee, D.E., 1991. Heating and thermal transformation of micrometeoroids entering the Earth's atmosphere. Icarus 89, 26–43.

Maurette, M., Immel, G., Hammer, C., Harvey, R., Kurat, G., Taylor, S., 1994. Collection and curation of IDPs from the Greenland and Antarctic ice sheets. In: Zolensky, M.E., Wilson, T.L., Rietmeijer, F.J.M., Flynn, G.J. (Eds.), Analysis of Interplanetary Dust Conference Proceedings. American Institute of Physics, Houston, pp. 277–289.

McDonough, W.F., Sun, S.-s., 1995. The composition of the Earth. Chem. Geol. 120, 223–253.

Milley, E.P., Hawkes, R.L., Ehrman, J.M., 2007. Meteor luminosity simulation through laser ablation of meteorites. Mon. Not. R. Astron. Soc. Lett. 382, L67–L71.

Pittarello, L., Yamaguchi, A., Roszjar, J., Debaille, V., Koeberl, C., Claeys, Ph., 2019. To be or not to be oxidized: a case study of olivine behavior in the fusion crust of ureilite A 09368 and H-chondrites A 09004 and A 09502. In: Meteoritics & Planetary Science, accepted.

Ramdohr, P., 1967. Chromite and chromite chondrules in meteorites I. Geochim. Cosmochim. Acta 31, 1961–1967.

Ravel, B., Newville, M., 2005. ATHENA, ARTEMIS, HEPHAESTUS: data analysis for X-ray absorption spectroscopy using IFEFFIT. J. Synchrotron Radiat. 12, 537–541.

Rubin, A.E., 2003. Chromite-plagioclase assemblages as a new shock indicator; implications for the shock and thermal histories of ordinary chondrites. Geochim. Cosmochim. Acta 67, 2695–2709.

Rubin, A.E., Grossman, J.N., 2010. Meteorite and meteoroid: new comprehensive definitions. Meteorit. Planet. Sci. 45, 114–122.

Rubin, A.E., Fegley, B., Brett, R., 1988. Oxidation state in chondrites. In: Kerridge, J.F., Matthews, M.S. (Eds.), Meteorites and the Early Solar System. University of Arizona Press, Tucson, Arizona, pp. 488–511.

Schaefer, L., Fegley Jr, B., 2004. A thermodynamic model of high temperature lava vaporization on Io. Icarus 169, 216–241.

Shepard, C.E., Vorreiter, J.W., Stine, H.A., Winovich, W., 1966. A Study of Artificial Meteors as Ablators. 5th Congress of the International Council of the Aeronautical Sciences, London, England, Tech. Rep. NASA TN D-3740. In: https://ntrs.nasa.gov/archive/nasa/casi.ntrs.nasa.gov/19670010552.pdf.

Suttle, M.D., Genge, M.J., Folco, L., Van Ginneken, M., Lin, Q., Russel, S.S., Najorka, J., 2019. The atmospheric entry of fine-grained micrometeorites: the role of volatile gases in heating and fragmentation. Meteorit. Planet. Sci. https://doi.org/10.1111/maps.13220, (in press).

Taylor, S., Lever, J.H., Harvey, R.P., 1998. Accretion rate of cosmic spherules measured at the south pole. Nature 392, 899–903.

Taylor, S., Lever, J.H., Harvey, R.P., 2000. Numbers, types, and compositions of an unbiased collection of cosmic spherules. Meteorit. Planet. Sci. 35, 651–666.

Taylor, S., Alexander, C.M.O'D., Delaney, J., Ma, P., Herzog, G.F., Engrand, C., 2005. Isotopic fractionation of iron, potassium and oxygen in stony cosmic spherules: implications for heating histories and sources. Geochim. Cosmochim. Acta 69, 2647–2662.

Thaisen, K.G., Taylor, L.A., 2009. Meteorite fusion crust variability. Meteorit. Planet. Sci. 44, 871–878.

Thomas, R.N., White, W.C., 1953. The physical theory of meteors. 4th inquiry into the radiation – a laboratory model. Astrophys. J. 118, 555–566.

Toppani, A., Libourel, G., 2003. Factors controlling compositions of cosmic spinels: application to atmospheric entry conditions of meteoritic materials. Geochim. Cosmochim. Acta 67, 4621–4638.

Toppani, A., Libourel, G., Engrand, C., Maurette, M., 2001. Experimental simulation of atmospheric entry of micrometeorites. Meteorit. Planet. Sci. 36, 1377–1396.

van Ginneken, M., Gattacceca, J., Rochette, P., Sonzogni, C., Alexandre, A., Vidal, V., Genge, M.J., 2017. The parent body controls on cosmic spherule texture: evidence from the oxygen isotopic compositions of large micrometeorites. Geochim. Cosmochim. Acta 212, 196–210.

Whitney, D.L., Evans, B.W., 2010. Abbreviations for names of rock-forming minerals. Am. Mineral. 95, 185–187.

Wilke, M., Farges, F., Petit, P.E., Brown, G.E., Martin, F., 2001. Oxidation state and coordination of Fe in minerals: an Fe K-XANES spectroscopic study. Am. Mineral. 86, 714–730.

Wlotzka, F., 2005. Cr spinel and chromite as petrogenetic indicators in ordinary chondrites: equilibration temperatures of petrologic types 3.7 to 6. Meteorit. Planet. Sci. 40, 1673–1702.

Zotikov, I.A., 1959. An experimental study of fusion of bodies by a supersonic flow. Meteoritika 17, 85–92, (in Russian).